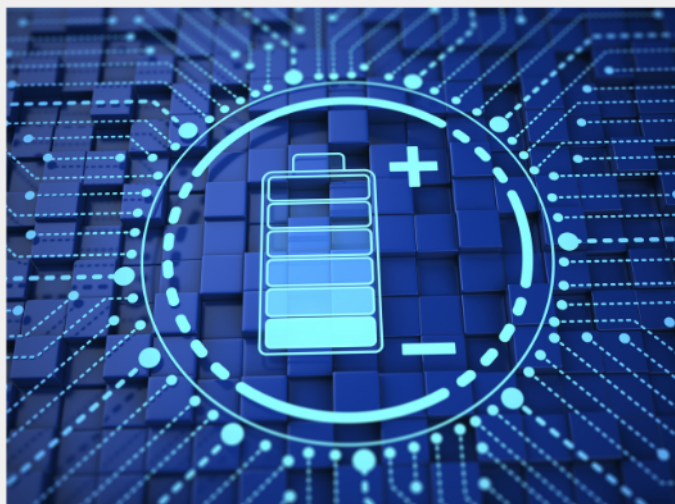




# Exploring the possibilities of increasing energy density and efficiency in rechargeable batteries

Download this complimentary article collection



The exponential rise in the need for better, more efficient power sources has sparked an incredible amount of research into batteries. A primary focus of research has been increasing the energy density of batteries, as it allows for lighter, more portable storage of energy. Lithium-ion batteries, for example, have a much higher energy density than conventional lead-acid batteries and can be used for various purposes, such as in electric vehicles.

This article collection provides a comprehensive list of references for new methods and technologies for increasing the energy density of batteries.

# The Exsolution of Cu Particles from Doped Barium Cerate Zirconate via Barium Cuprate Intermediate Phases

Mei Wang, Evangelos I. Papaioannou, Ian S. Metcalfe, Aaron Naden, Cristian D. Savaniu, and John T. S. Irvine\*

As a low-cost alternative to noble metals, Cu plays an important role in industrial catalysis, such as water-gas shift reaction, methanol or ethanol oxidation, hydrogenation of oils, CO oxidation, among many others. An important step in optimizing Cu catalyst performance is control of nanoparticles size, distribution, and the interface with the support. While proton conducting perovskites can enhance the metal catalytic activity when acting as the support, there has been limited investigation of in situ growth of Cu metal nanoparticles from the proton conductors and its catalytic performance. Here, Cu nanoparticles are tracked exsolved from an A-site-deficient proton-conducting barium cerate-zirconate using scanning electron microscopy, revealing a continuous phase change during exsolution as a function of reduction temperature. Combined with the phase diagram and cell parameter change during reduction, a new exsolution mechanism is proposed for the first time which provides insight into tailoring metal particles interfaces at proton conducting oxide surfaces. Furthermore, the catalytic behavior in the CO oxidation reaction is explored and, it is observed that these new nanostructures can rival state of the art catalysts over long term operation.

candidates in the field of heterogeneous catalysis as opposed to traditional noble-metal catalysts, owing to their lower cost and high activity for a variety of applications including reverse water gas shift reactions,  $\text{NH}_3$  synthesis,  $\text{CO}_2$  methanation, oxidative coupling of methane as well as automotive exhaust catalysis.<sup>[4–16]</sup> Specifically, CO oxidation applied in pollution control in automotive exhaust and air purification employs more than 60% of the annual production of noble metals, such as Pt.<sup>[17]</sup> When  $\text{ABO}_3$  perovskite-type oxides were used as catalyst supports for metal nanoparticles, those showed higher activities than those on the inert supports, such as  $\text{SiO}_2$  and  $\text{Al}_2\text{O}_3$ . The enhanced performance may come from the change of the acid-base properties of the catalysts, the dispersion of nanoparticles, and the interaction between the active particles and support.<sup>[18]</sup>


## 1. Introduction

$\text{ABO}_3$  perovskite-type oxides have been applied widely in sensors, solid oxide fuel cells, and solid oxide electrolysis cells, due to their advanced properties such as high ionic conductivity, high electronic conductivity, design flexibility and excellent chemical stability over a wide range of temperatures.<sup>[1–3]</sup> The  $\text{ABO}_3$  perovskite-type oxides were also found to be promising

Since proton conduction in perovskite oxides was firstly discovered by Iwahara in 1981,<sup>[19]</sup> it has opened new opportunities for electrochemical devices, such as chemical sensors, hydrogen separation,<sup>[20–22]</sup> hydrogenation and dehydrogenation of organic compounds,<sup>[23]</sup> electrolysers, and solid oxide fuel cells.<sup>[24–29]</sup> Particularly renowned in the fields of electrolysis and fuel cells, the great potential of proton conductors is due to the possibility of lowering their operating temperatures (<600 °C). The fuel and steam are supplied or produced at different electrodes, exempting from gas separation process. Catalytic activity of proton conducting perovskites is thus of great importance not only for chemical catalysis but also for the electro-catalysis when these materials are used as an electrode material in solid oxide cells. Among the various materials, acceptor-doped  $\text{BaZrO}_3$  and  $\text{BaCeO}_3$  are the state-of-the-art high temperature proton conductors. The catalytic activity of metal particles supported on the proton conducting oxides has previously been investigated, demonstrating promising properties. Shin et al.<sup>[8]</sup> investigated the catalytic performance for  $\text{CO}_2$  methanation of Pt decorated Co nanoparticle catalysts supported on the  $\text{BaZrO}_3$  and Y-doped  $\text{BaZrO}_3$  oxides, where the deposition of Co catalysts to the support was by a standard incipient wetness procedure. The results showed that catalysts supported on  $\text{BaZrO}_3$  had a  $\text{CH}_4$  formation rate of 6-fold higher than those on  $\gamma\text{-Al}_2\text{O}_3$  and a selectivity of 80% at 325 °C, in comparison to 43% for  $\gamma\text{-Al}_2\text{O}_3$  support. The catalytic activity promotion effect of proton-conducting oxide was also

M. Wang, A. Naden, C. D. Savaniu, J. T. S. Irvine  
School of Chemistry  
University of St Andrews  
St Andrews, Fife KY16 9ST, UK  
E-mail: jtsi@st-and.ac.uk

E. I. Papaioannou, I. Metcalfe  
School of Engineering  
Newcastle University  
Newcastle NE1 7RU, UK

 The ORCID identification number(s) for the author(s) of this article can be found under <https://doi.org/10.1002/adfm.202302102>.

© 2023 The Authors. Advanced Functional Materials published by Wiley-VCH GmbH. This is an open access article under the terms of the Creative Commons Attribution License, which permits use, distribution and reproduction in any medium, provided the original work is properly cited.

The copyright line for this article was changed on 27 April 2023 after original online publication.

DOI: 10.1002/adfm.202302102

observed in Ni catalyzing ammonia synthesis from hydrogen and nitrogen, where the specific activity of BaZr<sub>0.1</sub>Ce<sub>0.7</sub>Y<sub>0.2</sub>O<sub>3-δ</sub> (BCZY) supported Ni is ≈72 times higher than that of non-proton conducting MgO-CeO<sub>2</sub> supported catalysts.<sup>5</sup> The enhanced performance was suspected to be due to the proton conducting nature of the support.

In situ exsolution from perovskite has been found to be a very promising method to obtain metal nanoparticles.<sup>[30–32]</sup> By doping the catalytic active cation onto the B-site of the perovskite oxide under high temperature sintering, the targeted B-cation can be exsolved out as nanoparticles on the perovskite surface when subsequent chemical or electrochemical reduction is carried out at about 500–1000 °C. This can be regarded as a phase decomposition reaction, driven by reduction. Nanoparticles grown by exsolution exhibit strong stability and maintain high catalytic activity under various chemical environments during operation.<sup>[16,33–36]</sup> However, in many cases, except the preferred B-site metal nanoparticles, the large A-site cation, such as La<sup>3+</sup>, also precipitated on the perovskite surface in the form of La<sub>2</sub>O<sub>3</sub> or La(OH)<sub>3</sub>. By introducing A-site deficiency in the perovskite (A<sub>1-α</sub>BO<sub>3-δ</sub>), the tendency of A-site segregation can be weakened.<sup>[31]</sup>

Up to now, a variety of cations have been demonstrated to exsolve from perovskite oxide lattices through the in situ exsolution method,<sup>[37–43]</sup> and only limited research was involved in the exsolution from proton conducting barium cerate or zirconate oxides.<sup>[10,23,44–46]</sup> Although particle exsolution is observed in these studies, the particle growth mechanism is not well understood and remains unclear up to now. By understanding the exsolution process from a proton-conducting perovskite, the emerging phases end up with after reduction can be controlled and thus the materials properties can be tuned.

In this work, Cu doped A-site deficient BCZY was synthesized by solid state method, achieving the composition Ba<sub>0.95</sub>Ce<sub>0.5</sub>Zr<sub>0.3</sub>Y<sub>0.14</sub>Cu<sub>0.06</sub>O<sub>3-δ</sub> (denoted as BCZYC). A combination of XRD, scanning and transmission electron microscopies reveal a novel exsolution mechanism, where A-site segregation is not a barrier for Cu exsolving from the BCZYC but instead providing Cu nucleation sites by forming the eutectic as intermediate phase for Cu metal exsolution. Furthermore, as a preliminary proof of concept, the catalytic activity and stability of the prepared nanostructures were tested for the CO oxidation reaction in conditions relevant to emission control catalysis.<sup>[16,47]</sup>

## 2. Experimental Section

### 2.1. Sample Preparation and Processing

The BCZYC perovskite oxide was prepared by the solid-state synthesis. Precursor powders, BaCO<sub>3</sub> (Aldrich, >99%), CeO<sub>2</sub> (Sigma-Aldrich, >99.9%), ZrO<sub>2</sub> (Aldrich, >99%) and Y<sub>2</sub>O<sub>3</sub> (Alfa Aesar, >99.9%) were dried in air at 300 °C to remove absorbed H<sub>2</sub>O and CO<sub>2</sub> and weighed according to the stoichiometry of Ba<sub>0.95</sub>Ce<sub>0.5</sub>Zr<sub>0.3</sub>Y<sub>0.14</sub>Cu<sub>0.06</sub>O<sub>3-δ</sub> while warm. Powders were then dispersed in acetone and finely mixed by an ultrasonic probe (Herslcher UP200S) to break down agglomerates. Afterwards, the acetone was evaporated under continuous stirring, followed by calcination at 1000 °C for 12 h in air in a muffle furnace, with a ramping rate of 5 °C min<sup>-1</sup>. The pre-calcined oxides

were mixed with 6 mol% CuO (Sigma-Aldrich, >99%) by the ultrasonic probe in acetone and then dried in air. About 2.5 g powder was put into a steel die (ϕ = 2.3 cm) and pressed into pellets with a uniaxial press. The pellet was transferred on an alumina plate and sintered at 1350 °C for 12 h in air with a ramping rate of 5 °C min<sup>-1</sup>. A layer of the sintered perovskite powder was applied as a buffer layer between the alumina plate and pellet to avoid the reaction between them.

The segregation of the large A-site cation on the surface was found to be the most common phenomenon in stoichiometric perovskite due to the dangling bonds of the surface atoms.<sup>[48]</sup> Therefore, the cleaved surfaces were used to observe exsolution because they were more representative of the nominal bulk stoichiometry. In preparing a cleaved surface, the sintered pellet was fractured with a pestle in a mortar, and one piece of the pellet was transferred into tubular furnace supplied with dry 5% H<sub>2</sub>/Ar (25 ml min<sup>-1</sup>). The reduction temperature varied between 500–900 °C for 12 h with a ramping rate of 5 °C min<sup>-1</sup> (each reduction temperature was applied to different piece of pellet). In addition, a polished pellet surface was used to track the particle and phase evolution reduced at temperatures from 600 to 900 °C. Polishing was carried out with a Metaserv 2000 polisher, using MetPrep P600 and P1200 polishing paper, followed by MetPre 6, 3, and 1 μm cloth polishing with diamond paste.

### 2.2. CO Oxidation Tests

For the CO oxidation experiments a polished Cu-doped BCZY pellet was used. To exsolve particles, the pellet sample was reduced in a controlled atmosphere furnace, under continuous flow of 5% H<sub>2</sub>/Ar (25 ml min<sup>-1</sup>) at 600 °C for 12 h with heating and cooling rates of 5 °C min<sup>-1</sup>. The catalytic activity of the Cu-doped BCZY pellet was tested using in a continuous-flow single-chamber reactor. A K-type thermocouple was placed to close proximity of the pellet sample to measure the sample temperature during the reaction. All experiments were conducted at atmospheric pressure. Also, a fixed bed reactor filled with Al<sub>2</sub>O<sub>3</sub> powder was placed upstream to the single chamber reactor and was used to capture possible decomposed carbonyl species formed in the CO-containing gas cylinders. For the CO oxidation reaction, 20% CO/He, 20% O<sub>2</sub>/He, and CP grade He provided gases were used provided by BOC Ltd. Helium was used as a balance gas. Flow rates of 1 × 10<sup>-4</sup> mol s<sup>-1</sup> were used (at normal temperature and pressure, NTP). The flow rates were controlled using mass flow controllers and measured at the outlet using a 1000 series Varian digital flow meter. To study the effect of temperature on the reaction rate, the pellet sample was heated in an inlet gas composition of 1% of O<sub>2</sub> and 0.6% of CO from 100 to 520 °C. During heating in steps of 20 °C, the holding time had been varied depending on the time the reaction rate needed to stabilise (i.e., not vary >±5% for at least 60 min). To analyse the carbon dioxide (CO<sub>2</sub>) mole fraction in the product stream an XTREAM-CO<sub>2</sub> analyser provided by Rosemount was used. The minimum measurable CO<sub>2</sub> mole fraction for the XTREAM-CO<sub>2</sub> analyser was 1 ppm, which corresponds to a minimum measurable rate of CO<sub>2</sub> production of 1 × 10<sup>-10</sup> mol s<sup>-1</sup> with typical flow rate at 150 cm<sup>3</sup> min<sup>-1</sup> (1 × 10<sup>-4</sup> mol s<sup>-1</sup>). Reaction rates (*r*<sub>CO<sub>2</sub></sub>) in terms of steady CO<sub>2</sub> production rates were calculated as shown below in Equation 1:

$$r_{\text{CO}_2} = ((\text{mol of CO}_2)\text{s}^{-1}\text{cm}^{-2}) = Y_{\text{CO}_2} \cdot \dot{n} \cdot A^{-1} \quad (1)$$

where,  $Y_{\text{CO}_2}$  was the measured  $\text{CO}_2$  mole fraction at outlet gas stream,  $\dot{n}$  was the molar flow rate and  $A$  was the pellet surface area (top surface where exsolution took place). The reactor was operated under “gradientless” conditions (differential conversion of carbon monoxide (CO) of 25% or less). The CO conversion was calculated using Equation 2:

$$\text{CO conversion} = \frac{Y_{\text{CO}_2}}{Y_{\text{CO}}} \times 100 \quad (2)$$

where,  $Y_{\text{CO}}$  was the CO mole fraction at the reactor inlet.

In order to see how the site activities of the Cu particles compare to the literature, their nominal turnover frequency (nTOF) was calculated during the CO oxidation reaction. The nTOF was calculated as the number of molecules reacted per time (in seconds), per exposed metal atom site at the surface of particles, using Equation 3:

$$n\text{TOF}(\text{s}^{-1}) = 10^{-20} \cdot N_A \cdot r_{\text{CO}_2} \cdot a^2 / (A_e \cdot A_p \cdot k) \quad (3)$$

where,  $N_A$  was the Avogadro's number ( $\text{mol}^{-1}$ ),  $A_e$  was the surface area of the pellet decorated with particles per total surface area ( $\mu\text{m}^2 \mu\text{m}^{-2}$ ),  $A_p$  was the exposed particle area per total surface area ( $\text{cm}^2$ ),  $a$  was the unit cell parameter of the crystal lattice of the particles and  $k$  was the average number of metal sites per unit cell face (the faces were considered to be in a (100) termination, thus, for the CuO rock-salt structure  $k = 1$ ).

### 2.3. Sample Characterization

The crystallographic structure and crystalline phases of the perovskite were analysed by X-ray diffraction (XRD). The room temperature XRD (RT-XRD) patterns were collected on a PANalytical X-ray diffractometer in a  $2\theta$  range of  $10\text{--}90^\circ$  operating with  $\text{CuK}\alpha$  radiation ( $\lambda = 1.5406 \text{ \AA}$ ). The RT-XRD patterns were collected on powder sample, ground from the pellets with an agate pestle and a mortar. Variable temperature powder X-ray diffraction (VT-XRD) was used to in situ monitor solid phase transitions during reduction as a function of temperature, carried out on PANalytical Empyrean operating with Mo radiation ( $\lambda = 0.709 \text{ \AA}$ ) from  $10\text{--}45^\circ$  in  $5\% \text{ H}_2/\text{N}_2$ . The VT-XRD patterns were collected on a polished pellet.

The testing temperature profile was shown as **Figure 1**. Each temperature was held for 6 h and XRD pattern was collected every 2 h (3 times at each temperature) on heating, and only 1 h was held to collect the XRD data at each temperature during cooling down. Rietveld refinement of the X-ray data was analyzed using STOE WinXPOW software.

Surface morphology and phase homogeneity were investigated by SEM on a FEI Scios DualBeam microscope, equipped with secondary electron, backscattered electron detectors and an EDS analysis system. The samples were left uncoated.

TEM samples were prepared by focused ion beam (FIB), operated on Scios DualBeam microscopy. Protective carbon and platinum layers were first deposited onto the selected area

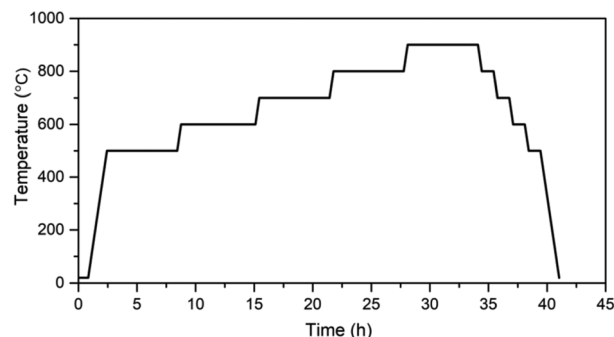


**Figure 1.** Temperature program of the VT-XRD test.

to prevent damage from the gallium focused ion beam. High-resolution transmission electron microscopy (HRTEM) was carried out on a probe-corrected Titan Themis STEM/TEM instrument operated at 200 kV.

## 3. Results and Discussion

### 3.1. Structural and Morphological Characterization of BCZYC Before Reduction

The crystalline structure of the as-prepared BCZYC material was examined by powder X-ray diffraction. As shown in **Figure 2a**, the sample exhibits a rhombohedral symmetry with space group R-3c. Minor impurities are detected labeled in the inset. The impurity phases are  $\text{Y}_2\text{BaCuO}_5$ ,  $\text{Y}_2\text{O}_3$ , and  $\text{Zr}_{0.9458}\text{Y}_{0.0545}\text{O}_{1.9732}$ , which commonly exist in the CuO aided sintering of barium cerate or zirconate.<sup>[49–53]</sup>

SEM image in **Figure 2b** reveals the microstructure of the native surface of BCZYC pellet. The sample shows a dense microstructure except for a few isolated pores. The shape of the grains is almost cuboid and forms a disordered grain boundary, suggesting an abnormal grain growth. Impurity phases are also found in the SEM images shown in **Figure S1a,b** (Supporting Information) and are characterized by EDS line scan and element quantitative analysis. These phases have been attributed to YSZ and  $\text{Y}_2\text{BaCuO}_5$ , in agreement with the XRD data.

### 3.2. Exsolution of the Cu Metal Particles from BCZYC

**Figure 3a–e** shows SEM images taken of cleaved pellets reduced at  $500\text{--}900^\circ\text{C}$  for 12 h. At each reduction temperature, large particles ( $\approx 0.2\text{--}1 \mu\text{m}$  diameter) can be seen often populating the grain boundaries and are labelled as *type I* particles (the particle size information is listed in Table 1) in **Figure 3a**. These particles become more spherical at higher reduction temperature and show a polyhedron morphology at  $900^\circ\text{C}$ . EDS quantitative result of spot 3 in **Figure S2** (Supporting Information) and EDS maps in **Figure 4a** show these particles to be Cu metal but with small amounts of Ba and O on the surface. Interestingly, thin platelet-like features can be seen underneath the Cu particles (highlighted in the yellow oval in **Figure 3c,d**) and they become island-like features at  $900^\circ\text{C}$ , existing at the interfacial area between the particles and the perovskite (**Figure 3e**).

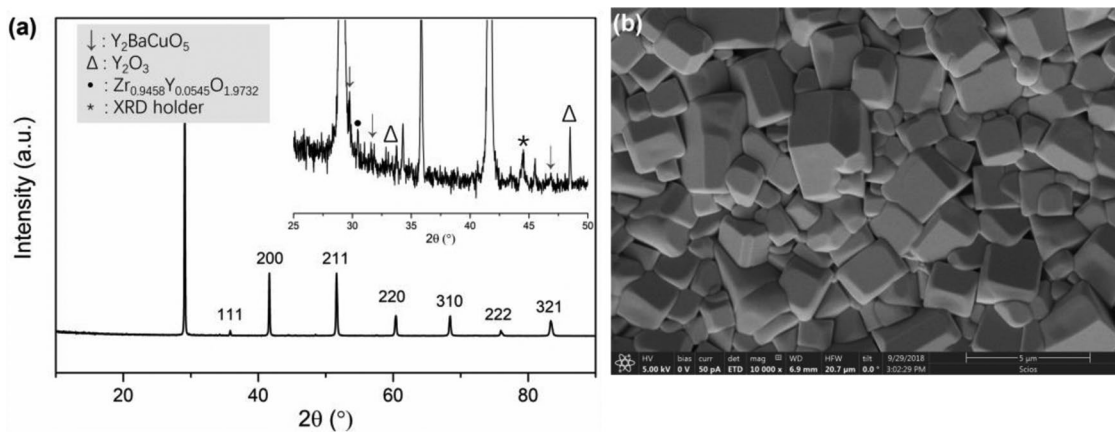


**Figure 2.** a) XRD pattern with the inset of higher magnification in the  $2\theta$  range of  $25\text{--}50^\circ$ , b) SEM image of the as-prepared  $\text{Ba}_{0.95}\text{Ce}_{0.5}\text{Zr}_{0.3}\text{Y}_{0.14}\text{Cu}_{0.06}\text{O}_{3-\delta}$  oxide sintered at  $1350^\circ\text{C}$  for 12 h.

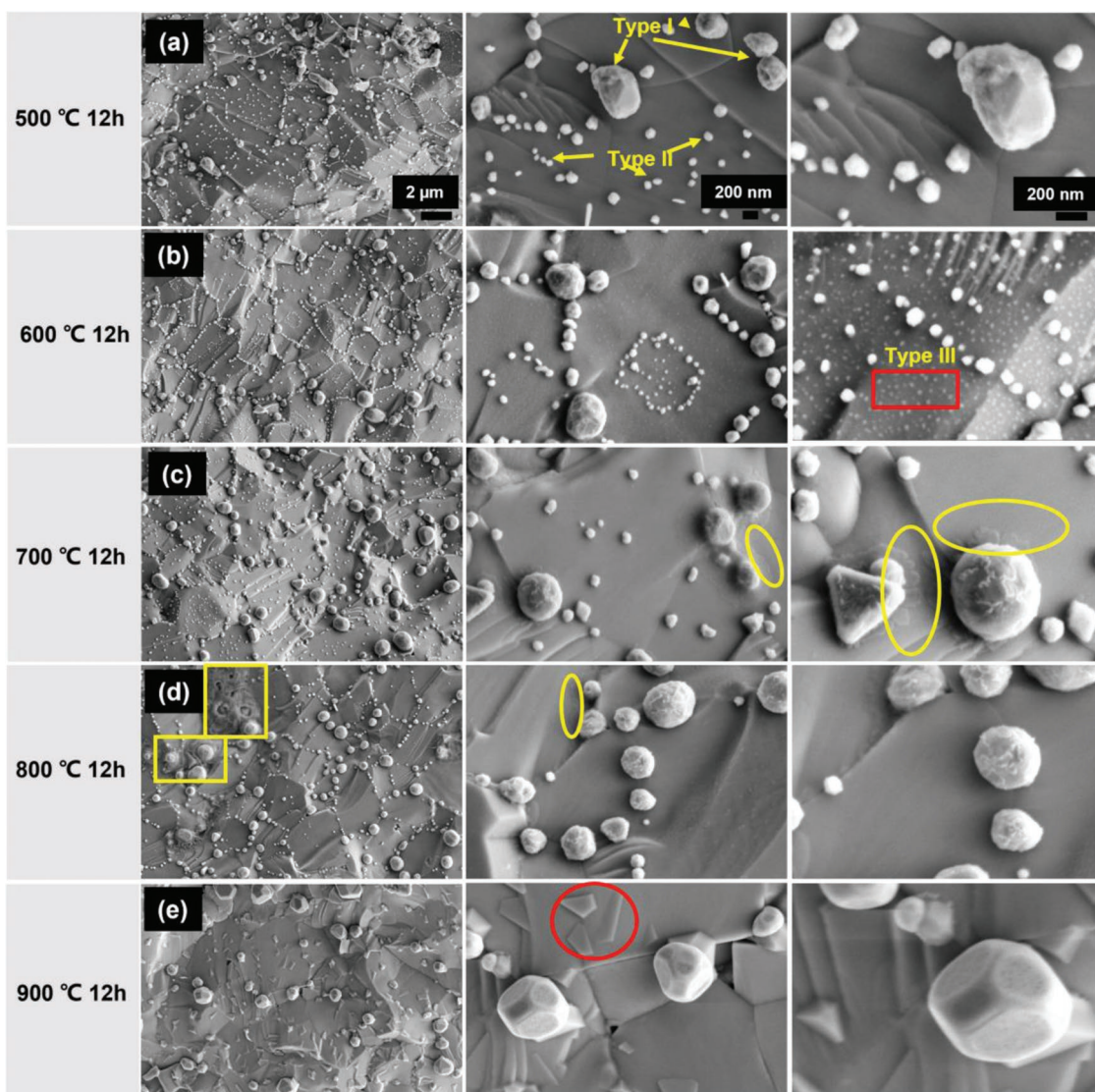


**Figure 3.** SEM images of cleaved surface of  $\text{Ba}_{0.95}\text{Ce}_{0.5}\text{Zr}_{0.3}\text{Y}_{0.14}\text{Cu}_{0.06}\text{O}_{3-\delta}$  pellet reduced at different temperatures for 12 h in 5%  $\text{H}_2/\text{Ar}$ , a)  $500^\circ\text{C}$ , b)  $600^\circ\text{C}$ , c)  $700^\circ\text{C}$ , d)  $800^\circ\text{C}$ , e)  $900^\circ\text{C}$ . The left, middle and right columns show magnification from low to high.

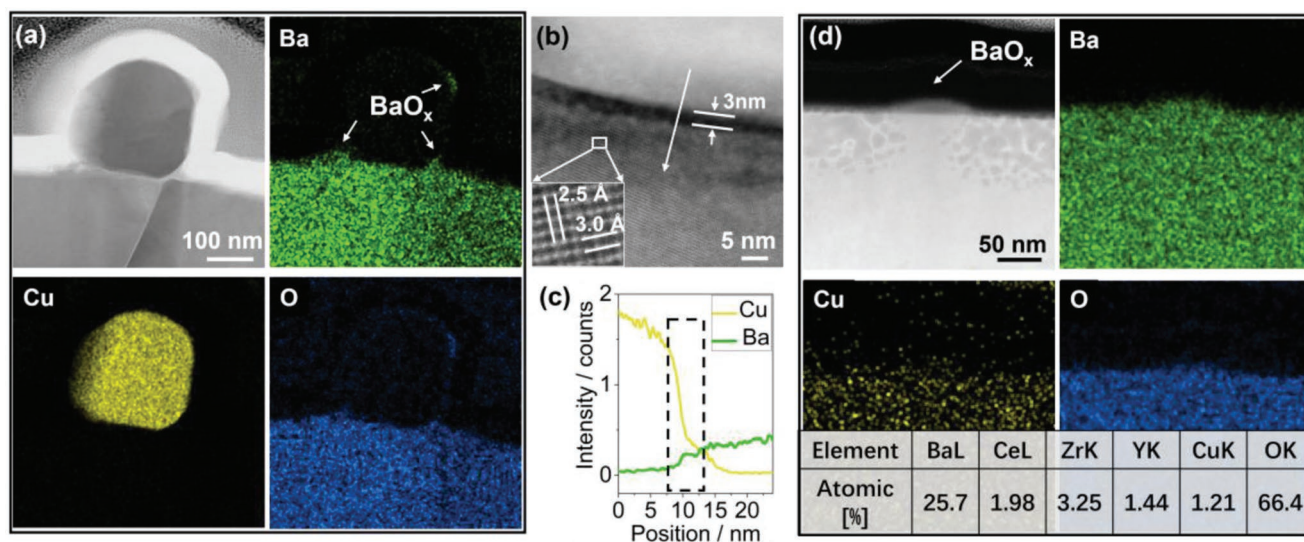


**Figure 4.** Characterization of the sample reduced at 900 °C for 12 h in 5% H<sub>2</sub>/Ar. a) HAADF image of the particles and its EDS maps of Ba, Cu and O elements, b) interface layer between the particle and the perovskite matrix in (a), the inset is the HR-TEM image of the bulk perovskite, c) EDS line scan profile along the arrow in (b), d) HAADF image and EDS maps of the “island” phase in Figure 3e, the inset table is the corresponding EDS quantification.

EDS maps in Figure 4a and Figure S4 (Supporting Information) reveal the phase cupping Cu particles is BaO<sub>x</sub>. From the line profile in Figure 4c, derived from region shown by the arrow in Figure 4b, this interfacial layer is revealed to have a thickness of ≈3 nm. The AO phase has also appeared in the Fe nanoparticles exsolution (adjacent to SrO nanorods) from La<sub>0.6</sub>Sr<sub>0.4</sub>FeO<sub>3-δ</sub> and Ni nanoparticles exsolution (adjacent to La<sub>2</sub>TiO<sub>5</sub>) from La<sub>0.43</sub>Ca<sub>0.37</sub>Ti<sub>0.94</sub>Ni<sub>0.06</sub>O<sub>3</sub>.<sup>[54,55]</sup> The similar island phases are also observed to socket alone without cupping particles at 900 °C (highlighted in the red circle in Figure 3e), suggested to be also BaO<sub>x</sub> from the EDS maps and quantification result in Figure 4d.

Apart from the large particles, smaller particles, labelled type II, with average size of ≈90 nm can also be observed in the temperature range of 500–800 °C (Figure 3a–d). They are less populated at higher temperature and almost only visible at the grain boundaries at 800 °C. The EDS quantification result of spot 1 in Figure S2 (Supporting Information) suggest the Type II particle contains mostly an amount of Cu with less Ba and Zr. It is possible that the Ba and Zr are from the matrix signal because the particle size is smaller than the electron beam effect area (The EDS penetration depth is ≈2 μm with a 20 keV electron beam).

Type III particles are the smallest ones (≈20 nm) and are only observed at reduction temperature of 600 °C, shown in the red square in Figure 3b). The EDS quantitative analysis in Figure S5 (Supporting Information) suggests a Ba-rich phase of the type III particle, and other elements except Ba from EDX are mainly due to fluorescence/projection effects. The type III particle is thus deduced to be BaO<sub>x</sub>. Treatment with O<sub>2</sub>/Ar plasma does not appear to affect their overall morphology (see Figure S3, Supporting Information), which also suggests a non-Cu metal particle phase of the type III particle. For the substrate area at EDS spot 4, the EDS quantitative result is almost identical to the Ba/Ce ratio present in Ba<sub>0.95</sub>Ce<sub>0.5</sub>Zr<sub>0.3</sub>Y<sub>0.14</sub>Cu<sub>0.06</sub>O<sub>3-δ</sub> but with less Zr and Y. No Cu was found in this area, suggesting that most Cu atoms have

already been stripped from the perovskite lattice due to the reduction treatment.

Occasionally, it is seen that the largest particles are wrapped in an extra phase highlighted in the yellow square region of Figure 3d. This extra phase can also be found on the pellets reduced at 500–700 °C but due to the limited observation area of the SEM they are not shown here. EDS quantitative analysis of spot 2 in Figure S2 (Supporting Information) indicates the excess amount of Ba and Cu in this phase compared with the perovskite substrate, supposed to be barium cuprate. They are probably formed from the impurity phase of Y<sub>2</sub>BaCuO<sub>5</sub> or from the reduction of the perovskite (Table 1).

### 3.3. Particle Tracking on Polished BCZYC Pellet

In contrast to the more conventionally observed “tidy” exsolution in the lanthanum titanate system, Cu exsolution from doped BCZY is accompanied with several types of phases, e.g., the “platelet-like” phase in the yellow oval and the “island” phase in Figure 3, making the exsolution process somewhat more complex. Particularly, it is still unclear whether the barium cuprate phase is formed from the perovskite lattice or a decomposition product of the Y<sub>2</sub>BaCuO<sub>5</sub> impurity phase. To exemplify the above, selected 12 regions of the Ba<sub>0.95</sub>Ce<sub>0.5</sub>Zr<sub>0.3</sub>Y<sub>0.14</sub>Cu<sub>0.06</sub>O<sub>3-δ</sub> perovskite pellet are shown in Figure 5, and their evolution with reduction temperature and duration is tracked. This pellet served as a well-defined model catalyst system for investigating the exsolution process.

**Table 1.** Particles type information.

Particles type	Type I	Type II	Type III
Particle size [nm]	≈200–1000	≈90	≈20

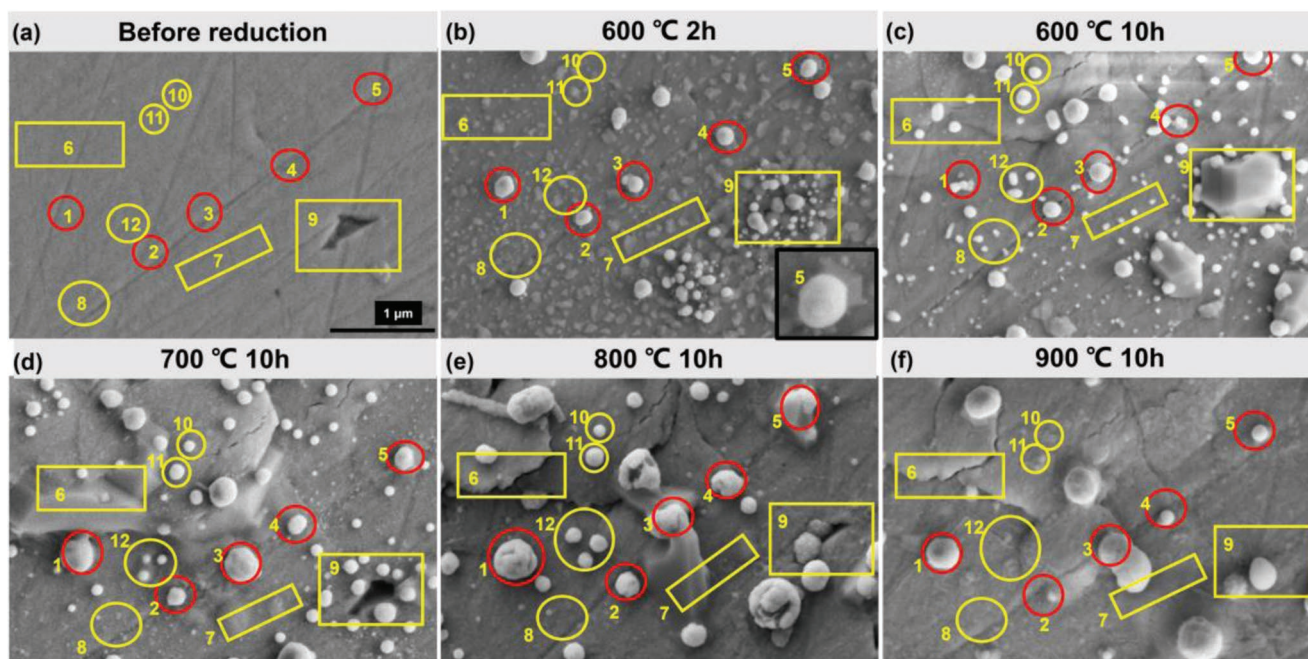


**Figure 5.** SEM images of the polished  $\text{Ba}_{0.95}\text{Ce}_{0.5}\text{Zr}_{0.3}\text{Y}_{0.14}\text{Cu}_{0.06}\text{O}_{3-\delta}$  pellet reduced at different temperature in 5%  $\text{H}_2/\text{Ar}$ , a) before reduction, b) 600 °C for 2 h, c) 600 °C for 10 h, d) 700 °C for 10 h, e) 800 °C for 10 h, f) 900 °C for 10 h. Note that each SEM image was taken at the same area after the pellet was reduced at each stage.

Before reduction, the pellet surface is clean with a defective hole at the area labeled 9. After reducing the pellet at 600 °C for 2 h (Figure 5b), some particles (e.g., particles 1, 2, 3, 4, 5) appear on the surface, believed to be the type I particle in Figure 3. A number of irregular-shaped phases are also present, e.g., at regions 6, 7, and 8, revealed to be  $\text{BaO}_x$  from the EDS maps in Figure 6b. Further reduction at 600 °C for 10 h, they evolve into spherical particles that could belong to the type II particles in Figure 3, with a smaller particle size ( $\approx 38$  nm) than those obtained after 2 h reduction ( $\approx 134$  nm). Therefore, the irregular-shaped phases ( $\text{BaO}_x$ ) seem to provide a transient stage for particle exsolution, we named them as “intermediate phase”. This kind of phase also exists underneath the spherical particles, such as in particle 5 in the inset of Figure 5b, and the nature of  $\text{BaO}_x$  is revealed by the TEM image in Figure 6c and EDS maps in Figure 6d and EDS quantification result in Figure 6e of spot 4. Also, the Cu particle is socketed in the  $\text{BaO}_x$  phase instead of the perovskite oxide. Another small Cu particle embedded in the  $\text{BaO}_x$  phase in Figure 6c is surrounded by some even smaller particles. Ba is shown to exist in the small Cu particle from the EDS quantification result of spot 3 and Ba EELS spectrum in Figure 6f. The dual composition in the particle is more obviously indicated from the BSE image in Figure S6b (Supporting Information). The Cu EELS spectrum in Figure 6g shows the  $\text{Cu}^0$  state with a small amount of  $\text{Cu}^{2+}$ , which may be due to the oxidation when handling the sample in air. For the perovskite bulk region 2 in Figure 6c, the EDS quantitative result illustrates a similar composition as the designed  $\text{Ba}_{0.95}\text{Ce}_{0.5}\text{Zr}_{0.3}\text{Y}_{0.14}\text{Cu}_{0.06}\text{O}_{3-\delta}$  but with less Cu that is resulted from its exsolution. At the defect of region 9 in Figure 5b, where it is accumulated with many particles and the  $\text{BaO}_x$  “intermediate phases” after reduction at 600 °C for

2 h, it evolves into a large irregular-shaped phase after another 10 h reduction (Figure 5c). EDS maps and quantitative result in Figure S7 (Supporting Information) indicate the existence of Ba, Cu, and O species in it, with relatively higher oxygen content than that in the parent perovskite, likely to be barium cuprate, which is also observed in Figure S2 (Supporting Information). The appearance of the barium cuprate phases also indicate they are formed from the perovskite lattice but not the reduction of  $\text{Y}_2\text{BaCuO}_5$  since no impurity phase exists at this area before reduction. With a series of reduction treatment at higher temperature (700–900 °C), similar kinds of large irregular phases keep decomposing and exsolving at some regions (region 6 in Figure 5d and region 7 at Figure 5e). They are all supposed to be barium cuprate but with different stoichiometry from 9 in Figure 5c, which is deduced from the previous microstructure observation in the study of  $\text{BaO}-\text{CuO}_x$  system.<sup>56</sup> Smaller particles seem to slowly re-dissolve into the perovskite substrate at temperatures higher than 700 °C (such as particles 2, 7, 8, 10, 11, and 12), gradually decreasing the particle population. The particles distribution variation can be seen in Figure S8 (Supporting Information) that the population decreases from  $18 \mu\text{m}^2$  at 600 °C to  $2 \mu\text{m}^2$  at 900 °C and the average particles size increases with temperature except at 700 °C when the smaller particle size is due to the partially re-dissolving into the perovskite.

#### 3.4. Analysis with Phase Diagram of BaO-CuO System

The Cu exsolution process from BCZY seems to be very complex, with several phases evolving on the surface, especially the re-dissolving of Cu particles and frequently observed barium

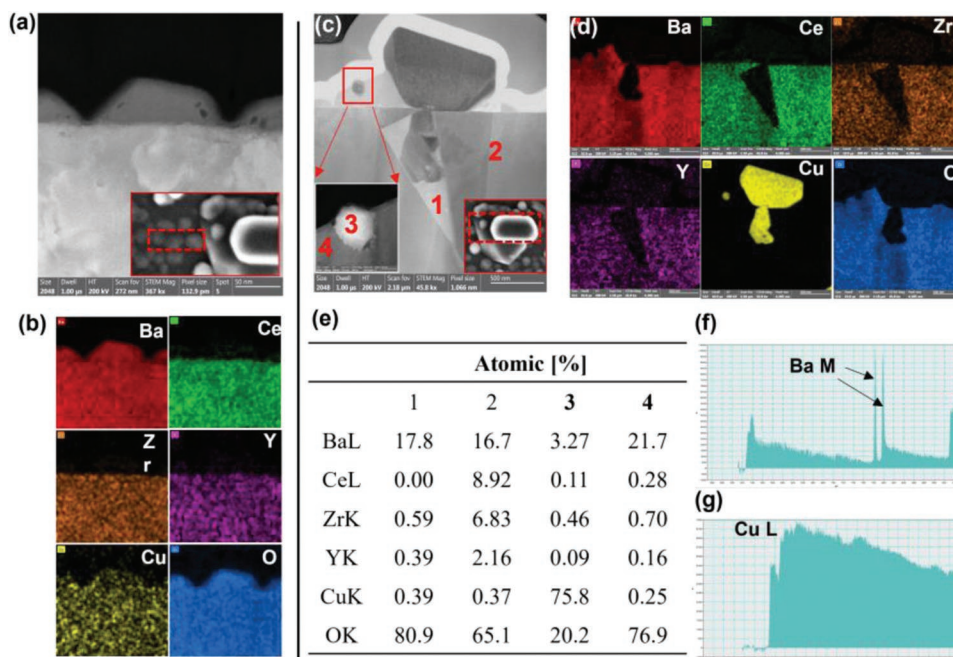
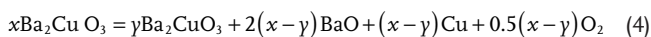


**Figure 6.** TEM characterization of the polished  $\text{Ba}_{0.95}\text{Ce}_{0.5}\text{Zr}_{0.3}\text{Y}_{0.14}\text{Cu}_{0.06}\text{O}_{3.8}$  sample reduced at  $600\text{ }^{\circ}\text{C}$  for 2 h in 5%  $\text{H}_2/\text{Ar}$ . a) TEM image and b) EDS maps of the intermediate phase, the inset is the SEM image of the sample for FIB preparation; c) the TEM image and d) EDS mappings of the particle with irregular shaped phase, the inset in (c) at the left bottom is the magnified TEM image of the particle in red square and the inset at the right bottom is the SEM image of the TEM sample; e) EDS quantification results of area 1, 2, 3, and 4 in (c); f, g) are the Ba and Ce EELS spectra in the small particle of region 3 in (c), respectively.

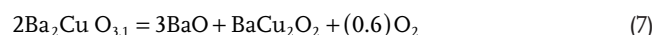
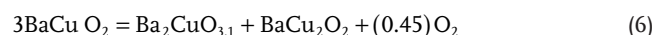
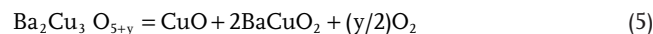
cuprate and  $\text{BaO}_x$  phases. Moreover, the suspected barium cuprate phases with different stoichiometries due to the varied reduction temperature further motivates us to know the phase equilibrium between  $\text{BaO}$  and  $\text{CuO}$ . Figure 7a presents the phase equilibrium of the  $\text{BaO}$ - $\text{CuO}$  system in air.<sup>[57–60]</sup> Since in our material, the amount of Ba is far more than Cu (Ba is  $\approx 15.8$  times of Cu amount), here we firstly analyze the Ba-rich region ( $\text{BaO} > 66.7\text{ mol}\%$ ) of the phase diagram. The schematic of phase change is illustrated in Figure 7b according to the phase diagram in Figure 7a. In order to simplify the analysis, we first assume that the phase equilibrium in the reducing atmosphere is the same as the one in air and the reduction temperature is held at  $800\text{ }^{\circ}\text{C}$ . Therefore, Cu will exsolve from the  $\text{Ba}_2\text{CuO}_3$  compound that is in equilibrium with  $\text{BaO}$  at this temperature. The Cu exsolution process will be accompanied with precipitation of  $\text{BaO}$ , otherwise a phase with richer Ba than 2:1 will be obtained, which disobeys the phase equilibrium at  $800\text{ }^{\circ}\text{C}$ . This process can be expressed as Equation 4 and illustrated in Figure 7c.



With exsolution progresses,  $\text{BaO}$  proportion in the  $\text{BaO}$ - $\text{CuO}$  system increases, leading to the phase equilibrium left shift parallelly until a limit value of pure  $\text{BaO}$ , following the blue arrow in Figure 7a. However, if the process of Cu exsolution from  $\text{Ba}_2\text{CuO}_3$  is slow,  $\text{Ba}_2\text{CuO}_3$  will not decompose completely when the temperature is held at  $800\text{ }^{\circ}\text{C}$  for 12 h. This will lead to a continuous decomposition during cooling as long as the temperature is high enough for the decomposition reac-

tion. In this case, the equilibrium on cooling does not follow a vertical line but a line with a positive slope (following the red arrow in Figure 7a). This process will finish until a temperature at which the exsolution is thermodynamically limited and followed by a vertical change in phase equilibrium at low temperature. Therefore, the incomplete decomposition of  $\text{Ba}_2\text{CuO}_3$  finally gives rise to a mixture of  $\text{BaO}_2$  and  $\text{Ba}_2\text{CuO}_3$  at room temperature. This may well explain why we observe the barium cuprate phases rich in oxygen in Figure S4 (Supporting Information).

The above analysis is based on the assumption that the phase equilibrium in reducing atmosphere is the same as that in air. However, the real equilibrium is changed with oxygen partial pressure. As shown in Figure S9 (Supporting Information), the compositions that can bear the  $P(\text{O}_2)$  from high to low is  $\text{Ba}_2\text{Cu}_3\text{O}_5$ ,  $\text{Ba}_2\text{CuO}_3$ ,  $\text{BaCuO}_2$  and  $\text{BaCu}_2\text{O}_3$ , respectively. The conversion between these phases in the  $\text{Ba}$ - $\text{Cu}$ - $\text{O}$  system is related to the following reactions:





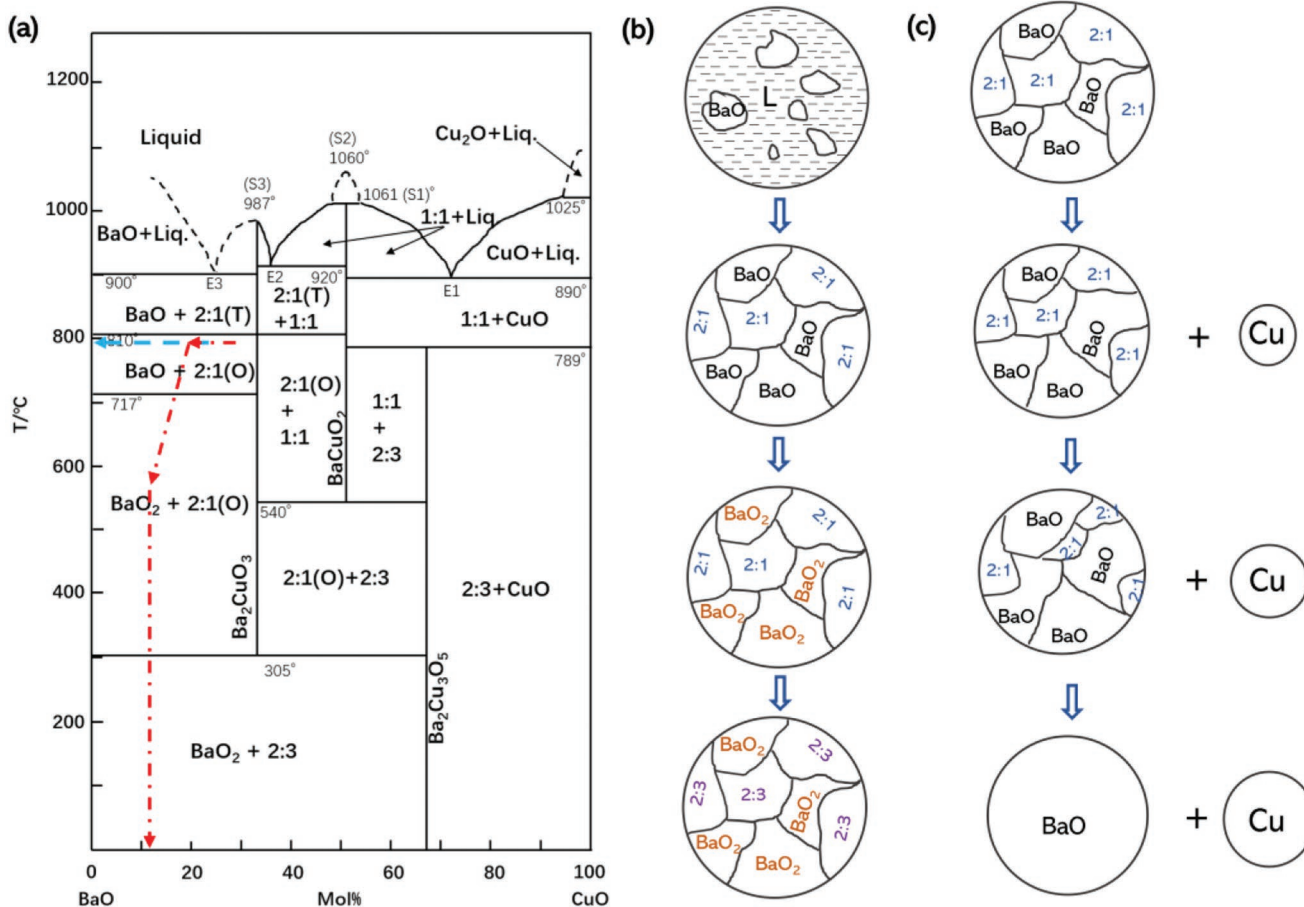


**Figure 7.** a) Phase diagram of BaO-CuO system, b) schematic of phase change on cooling in the BaO rich region ( $\text{BaO} > 66.7 \text{ mol}\%$ ) in air, c) schematic of phase change on cooling in the BaO rich region ( $\text{BaO} > 66.7 \text{ mol}\%$ ) in 5%  $\text{H}_2/\text{Ar}$  at 800 °C. The blue line indicates the phase change if barium cuprate phase can completely decompose at 800 °C, and the red line indicates the phases in equilibrium under the assumption that barium cuprate cannot decompose completely at 800 °C.

Under even lower  $P(\text{O}_2)$ , the  $\text{Cu}_2\text{O}$  and BaO can be reduced into the corresponding metal state by the Equation 1–7 and 1–8:



However, it is worth to mention that the phase diagram can only express thermodynamically instability of a phase and does not offer kinetic information, which means that it is unknown how quickly the unstable phase decomposes. This indicates that although the  $P(\text{O}_2)$  in our experiment may reach a value of  $10^{-29}$ , the Ba-Cu-O phase is possible to exist, and the  $\text{BaO}_2$  phase can also be present. In addition, the migration of lattice  $\text{Cu}^{2+}$  towards the surface and re-dissolving into the perovskite at high temperature may cause a local composition change. All these factors will result in a different Ba-Cu-O system but not only the Ba-rich one we discussed above. On reheating the pellet at higher temperature, the previously formed barium cuprate phase has enough time for decomposition, while at some regions a new barium cuprate phase is prone to be produced, as observed in Figure 5. Apparently, the

higher reheating temperature and the local composition change due to ions migration will give rise to the different Ba fraction in the barium cuprate phase, which is verified from the varied morphologies in the keep arising large irregular-shaped phase in Figure 5. Although the “intermediate phase” on the polished surface reduced at 600 °C for 2 h (Figure 5b) is indicated to be  $\text{BaO}_x$  by the TEM analysis, it is believed that lattice  $\text{Cu}^{2+}$  would diffuse towards the  $\text{BaO}_x$  phase to form Ba-Cu-O system if the sample is reduced for a longer time.

In Figure 3c,d, we observed the layered morphology of the nanoparticles and it is attributed to the involvement of eutectic solidification process. When the eutectic phase is formed at 890–920 °C (E1, E2, and E3) according to the phase diagram under air in Figure 7a, it is possible that the transformation temperature to eutectic decreases under reducing atmosphere. The thin layer in the yellow oval of Figure 3c,d could also indicate the participation of eutectic phase during reduction.

Overall, Cu exsolving from the doped barium cerate zirconate oxide by two steps: the exsolution of barium cuprate phase from the perovskite and the exsolution of Cu particles from the barium cuprate phase. This process is illustrated as the schematic in Figure 8. At lower reduction temperature

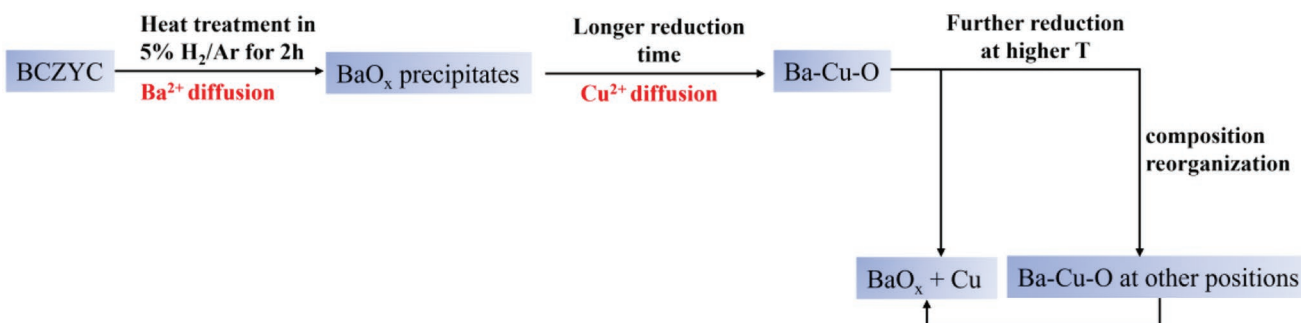


**Figure 8.** Schematic of Cu exsolution process from barium cerate zirconate oxide.

and short time, i.e., 600 °C for 2 h,  $\text{Ba}^{2+}$  first exsolves on the perovskite surface in the form of  $\text{BaO}_x$  (Figure 5b), lowering the migration barrier for the following  $\text{Cu}^{2+}$  migration with further reduction. Also, the pre-existed  $\text{BaO}_x$  enables the heteronucleation of Cu that is energy saving process, forming a Ba-Cu-O system (Figures S2,S7, Supporting Information). At higher reduction temperature, Cu particle is exsolved from the barium cuprate phase, producing  $\text{BaO}_x$  at the same time due to the decomposition reaction (Figure 3e). The lattice ions diffusion towards the surface, the re-dissolving of particles to the perovskite, and the exsolution of particles from barium cuprate make the local composition to reorganize, and thus producing a new Ba-Cu-O system in other regions (irregular-shaped phase in Figure 5c,d,e).

Herein, although B-site exsolution accompanied by A-site enrichment on the surface has been proposed, and BaO surface enrichment was found by TEM observation after Ni exsolution from  $\text{Ba}(\text{Zr}_{0.4}\text{Ce}_{0.4}\text{Y}_{0.2})_{0.8}\text{Ni}_{0.2}\text{O}_{3-\delta}$ <sup>[32,61]</sup> to the best of authors knowledge the phenomenon of co-segregation of A and B-site in the form of eutectic oxide has not been reported before. As previously reported, the A-site cation diffusion to the surface

filling the A-site vacancy creates a new rigid “native surface”, which is expected to prevent further diffusion of exsolvable cations and contribute to locking the particles into place. In our work, the co-segregation of Ba cation with Cu in the form of eutectic is more like to play a role in providing an energy-saving route for the B-site exsolution but not produce a hindering effect.

### 3.5. VT-XRD Analysis

VT-XRD experiment was conducted on the polished BCZYC pellet to investigate phase and cell parameter change with reduction and further reflect on the copper exsolution process. The perovskite peaks are indexed with the cubic symmetry in **Figure 9**. Two distinct peaks at 19.45° and 22.47° appears after reduction at 600 °C for 2 h, corresponding to the (111) and (200) plane of Cu metal, respectively. The peak intensity of Cu metal only increases slightly with reduction temperature and duration, indicating that the nucleation process may be time-dependent, but the growth of Cu is relatively fast.<sup>[54]</sup> In

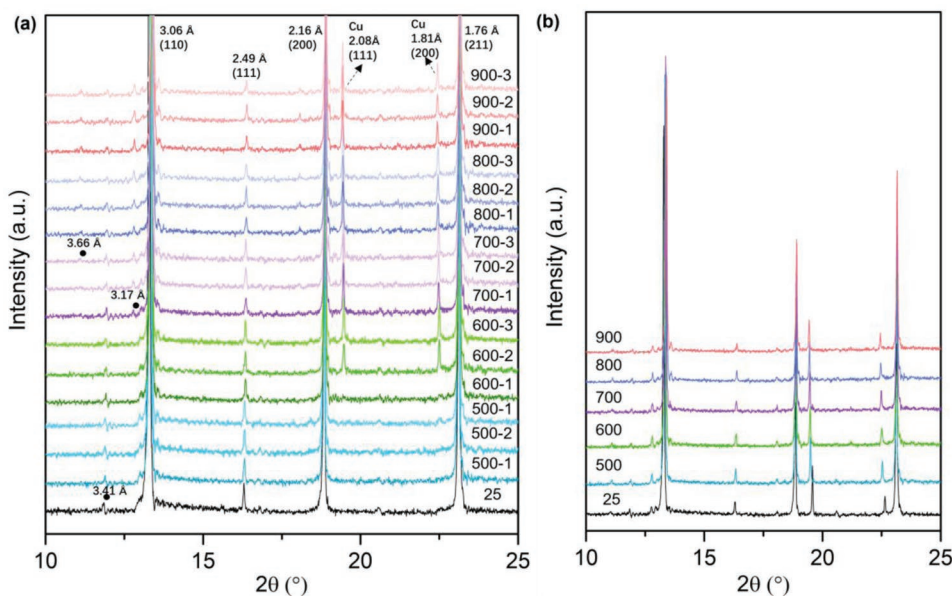


**Figure 9.** VT-XRD results of polished  $\text{Ba}_{0.95}\text{Ce}_{0.5}\text{Zr}_{0.3}\text{Y}_{0.14}\text{Cu}_{0.06}\text{O}_{3-\delta}$  pellet on heating a) and on cooling b) in 5%  $\text{H}_2/\text{N}_2$ . (Patterns are collected with  $\text{MoK}\alpha$  radiation, and a shoulder may be observed at each peak due to the stripping of peaks from  $\text{MoK}\alpha 2$ ).

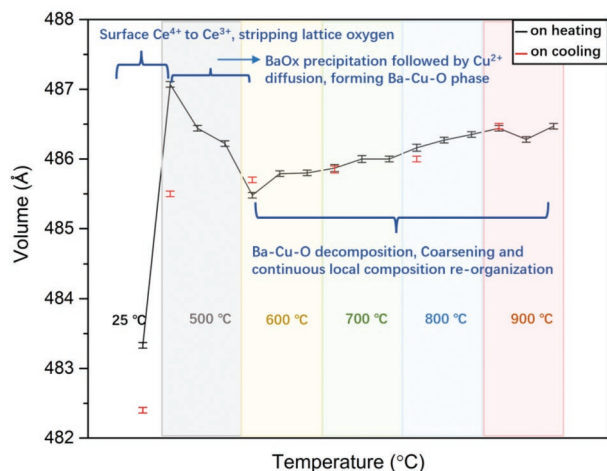


**Figure 10.** Cell volume of the polished BCZYC pellet on heating and on cooling calculated by the Rietveld refinement of VT-XRD patterns. The black graph is the cell volume on heating with XRD collected for three times at each reduction temperature, and the red symbols are the cell volume on cooling. The symbol size of the data implies the error.

addition, another two weak peaks at  $11.17^\circ$  and  $12.85^\circ$  appear at  $700^\circ\text{C}$ , corresponding to the  $\text{mZrO}_2$  phase according to the matched file data PDF #01-074-0815, which may come from the decomposition of the impurity phases. During cooling, there is no apparent evidence for the phase change in Figure 9b.

Since exsolution is an ion stripping process, unit cell constant would be changing along with the exsolution process. As Figure 10 displayed, the BCZYC pellet exhibits a maximum unit cell volume after reduction at  $500^\circ\text{C}$  for 2 h, resulting from the reduction of surface  $\text{Ce}^{4+}$  to  $\text{Ce}^{3+}$  on the one hand (with ionic radius increasing from 0.87 to 1.01 Å for six-fold coordinated cerium) and the stripping of lattice oxygen on the other hand. A rapid cell contraction occurs with further reduction until reduction at  $600^\circ\text{C}$  for 2 h, which is supposed to come from the massive diffusion of  $\text{Ba}^{2+}$  to form  $\text{BaO}_x$  on the surface and the followed  $\text{Cu}^{2+}$  migration, consistent with the SEM observation in Figure 5b. After that, further reduction at  $600^\circ\text{C}$  and even higher temperature to  $900^\circ\text{C}$  led to the slowly cell expansion, attributed mainly from the thermal expansion of the structure since almost the same tendency is observed in the cell volume on cooling. This vibration of unit cell volume is well reflected on the observation in Figure 5c–f that only mild evolution of the barium cuprate and particle coarsening occur in this period without considerable cation diffusion to the surface that can produce a significant change in the cell volume.

It is noticed that on cooling the cell volume remains similar at temperature between  $600$  and  $900^\circ\text{C}$  as those on heating, however, at  $500^\circ\text{C}$ , it did not change back to the value on heating. This indicates that the segregated Ba species is not able to re-incorporate into the perovskite structure.

### 3.6. Catalytic Activity and Stability Tests

A reduced Cu-doped BCZY pellet was tested for the CO oxidation reaction, as a preliminary proof of concept. The catalytic activity of the Cu-doped BCZY pellet sample was tested for

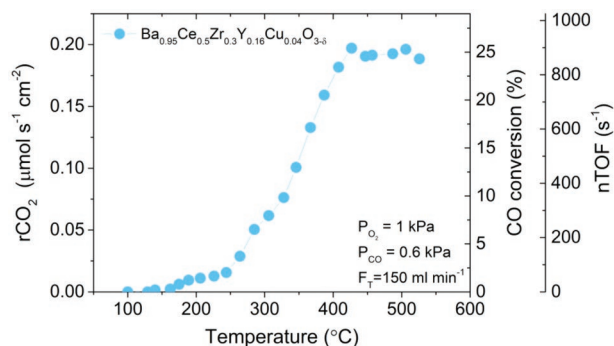


**Figure 11.**  $\text{CO}_2$  production rate as a function of temperature from CO oxidation test on Cu-doped BCZY pellet reduced at  $600^\circ\text{C}$  for 12 h. The right axes show the CO conversion and nTOF values as a function of temperature. Errors are of the size of the points used for plotting.

CO oxidation reaction under mildly oxidizing feed gas conditions (1%  $\text{O}_2$ , 0.6% CO), which are characteristic of catalytic converters,<sup>[16,62]</sup> as a function of temperature. Figure 11 shows the  $\text{CO}_2$  production rate ( $r_{\text{CO}_2}$ ) as a function of temperature on the left y-axis and the corresponding CO conversion and nTOF values as a function of temperature (right y-axes). It should be noted that the  $r_{\text{CO}_2}$  on the left y-axis is normalized with respect to the pellet surface area decorated with particles. As shown in Figure 11, the minimum temperature for any measurable  $\text{CO}_2$  reaction rate was around  $150^\circ\text{C}$  while above this temperature, the activity increased upon increasing temperature up to  $\approx 425^\circ\text{C}$  that corresponds to  $\approx 25\%$  of CO conversion. Above this temperature the  $\text{CO}_2$  reaction rate seems to be reaching a plateau. In order to compare the active site activities of the Cu-doped BCZY catalyst system to the literature for base metal exsolved systems and catalyst systems made by conventional deposition techniques, we calculate the nTOFs for the CO oxidation reaction. In order to do that, we assume that one active site corresponds to one surface metal atom and the nanoparticles have hemispherical shape.<sup>[16,63,64]</sup> Consistent with previous reports on thermally exsolved base metal nanoparticles, the nTOFs for the CO oxidation reaction are of the order of hundreds per second, with values up to  $900\text{ s}^{-1}$  at  $\approx 425^\circ\text{C}$ . That is a few orders of magnitude higher than generally reported for typical base metal or metal oxide nanoparticles produced through common deposition techniques and in the range typically reported for noble metal particles.<sup>[16,63]</sup> According to reports in literature, the high activity observed in exsolved nanoparticles from perovskite oxide supports as opposed to systems with nanoparticles deposited by traditional techniques (i.e., chemical impregnation) is attributed to the strain imposed by the sock-eting nature of these nanostructures.<sup>[64,65]</sup>

To investigate the long-term stability of the Cu-doped BCZY catalyst we measured the catalytic activity over a period of 170 h of continuous operation at  $520^\circ\text{C}$  (Figure 12). That is conditions where base metal nanoparticle catalysts produced by conventional methods typically deactivate via agglomerate within a few hours, even though are of practical importance in base metal catalysis.<sup>[66]</sup> It is worth noting that in the long-term stability test the same pellet sample that was used for the light-off experiment was employed. It can be seen that the  $\text{CO}_2$  reaction rate of the Cu-doped BCZY sample improved over the first 40 h

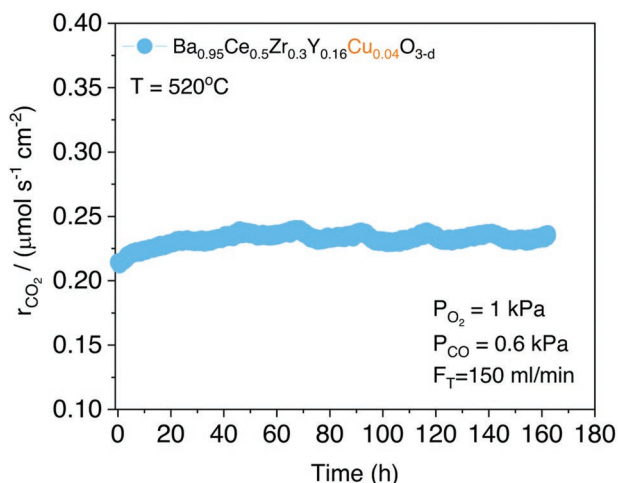


**Figure 12.** CO<sub>2</sub> production rate as a function of time on Cu-doped BCZY pellet, over 160 h at 520 °C.

of testing and was maintained over the remaining testing time, in agreement with similar reports on exsolved base metal catalyst systems.

#### 4. Conclusions

A large number of Cu particles was successfully formed by in situ exsolution from the proton-conducting BCZY perovskite. Individual particles are followed during their evolution with reduction temperature and duration, revealing a distinct exsolution process from the conventional one. The A-site Ba cations play a key role in the Cu exsolution process determined by the phase equilibrium of the BaO-CuO system. The first segregated BaO<sub>x</sub> species lowers the followed Cu<sup>2+</sup> migration barrier and provides the heteronucleation sites which is an energy saving path for Cu<sup>2+</sup> segregation. The formed barium cuprate eutectic phase acts as an intermediate phase for Cu particles exsolution. The BCZY supported Cu particles show excellent catalytic activity in CO oxidation reaction and have an nTOF value of 900 s<sup>-1</sup> at 425 °C and an outstanding long-term stability in a continuous test for 170 h.

#### Supporting Information

Supporting Information is available from the Wiley Online Library or from the author.

#### Acknowledgements

This research was supported by EPSRC research grants EP/R023522/1, EP/T019298/1, EP/R023751/1, EP/L017008/1 the China Scholarship Commission (MW) received financial support from the UK Catalysis Hub funded by EPSRC Grant reference EP/R027129/1.

#### Conflict of Interest

The authors declare no conflict of interest.

#### Data Availability Statement

The data that support the findings of this study are available at DOI 10.17630/de53f152a31f4coc9ee9-89aeecc2d27f.

#### Keywords

CO oxidation, eutectic, exsolution, nanoparticles, phase diagrams, proton conductors

Received: February 28, 2023

Published online:

- [1] R. Voorhoeve, D. Johnson, J. Remeika, P. Gallagher, *Science* **1977**, 195, 827.
- [2] Y.-F. Y. Yao, *J. Catal.* **1975**, 36, 266.
- [3] M. Pena, J. Fierro, *Chem. Rev.* **2001**, 101, 1981.
- [4] C. H. Kim, G. Qi, K. Dahlberg, W. Li, *Science* **2010**, 327, 1624.
- [5] J. Humphreys, R. Lan, D. Du, W. Xu, S. Tao, *Int. J. Hydrogen Energy* **2018**, 43, 17726.
- [6] V. O. Igenegbai, R. J. Meyer, S. Linic, *Appl. Catal., B* **2018**, 230, 29.
- [7] J. Lin, Z. Wang, L. Zhang, J. Ni, R. Wang, K. Wei, *Chin. J. Catal.* **2012**, 33, 1075.
- [8] H. H. Shin, L. Lu, Z. Yang, C. J. Kiely, S. McIntosh, *ACS Catal.* **2016**, 6, 2811.
- [9] D. H. Kim, J. L. Park, E. J. Park, Y. D. Kim, S. Uhm, *ACS Catal.* **2014**, 4, 3117.
- [10] U. Singh, J. Li, J. Bennett, A. Rappe, R. Seshadri, S. Scott, *J. Catal.* **2007**, 249, 349.
- [11] W. Libby, *Science* **1971**, 171, 499.
- [12] H. Tanaka, M. Taniguchi, M. Uenishi, N. Kajita, I. Tan, Y. Nishihata, J. i. Mizuki, K. Narita, M. Kimura, K. Kaneko, *Angew. Chem., Int. Ed.* **2006**, 45, 5998.
- [13] H. Tanaka, N. Mizuno, M. Misono, *Appl. Catal., A* **2003**, 244, 371.
- [14] B. Seyfi, M. Baghalha, H. Kazemian, *Chem. Eng. J.* **2009**, 148, 306.
- [15] S. Royer, D. Duprez, F. Can, X. Courtois, C. Batiot-Dupeyrat, S. Laassiri, H. Alamdari, *Chem. Rev.* **2014**, 114, 10292.
- [16] D. Neagu, E. I. Papaioannou, W. K. W. Ramli, D. N. Miller, B. J. Murdoch, H. Menard, A. Umar, A. J. Barlow, P. J. Cumpson, J. T. S. Irvine, I. S. Metcalfe, *Nat. Commun.* **2017**, 8, 1855.
- [17] S. Wang, A. Chen, Z. Zhang, J. Peng, *Environ. Prog. Sustainable Energy* **2014**, 33, 913.
- [18] M. Seo, S. Y. Kim, Y. D. Kim, E. D. Park, S. Uhm, *Int. J. Hydrogen Energy* **2018**, 43, 11355.
- [19] H. Iwahara, T. Esaka, H. Uchida, N. Maeda, *Solid State Ionics* **1981**, 3, 359.
- [20] M. Liu, W. Sun, X. Li, S. Feng, D. Ding, D. Chen, M. Liu, H. C. Park, *Int. J. Hydrogen Energy* **2013**, 38, 14743.
- [21] Q. A. Islam, M. W. Raja, R. N. Basu, *J. Am. Ceram. Soc.* **2017**, 100, 1360.
- [22] S. Fang, K. S. Brinkman, F. Chen, *J. Membr. Sci.* **2014**, 467, 85.
- [23] J. Basu, A. Suresh, B. A. Wilhite, C. B. Carter, *J. Eur. Ceram. Soc.* **2011**, 31, 1421.
- [24] H. Iwahara, *Solid State Ionics* **1996**, 86, 9.
- [25] H. Iwahara, H. Uchida, J. Kondo, *J. Appl. Electrochem.* **1983**, 13, 365.
- [26] T. Hibino, A. Hashimoto, K. Mori, M. Sano, *Electrochem. Solid-State Lett.* **2001**, 4, H9.
- [27] H. Iwahara, H. Uchida, K. Morimoto, *J. Electrochem. Soc.* **1990**, 137, 462.
- [28] N. Bonano, B. Ellis, M. Mahmood, *Solid State Ionics* **1991**, 44, 305.
- [29] B. C. Steele, A. Heinzel, *Materials for fuel-cell technologies. In Materials for sustainable energy: a collection of peer-reviewed Research and*

- review articles from nature publishing group, World Scientific, Singapore **2011**, pp. 224–231.
- [30] Y. Nishihata, J. Mizuki, T. Akao, H. Tanaka, M. Uenishi, M. Kimura, T. Okamoto, N. Hamada, *Nature* **2002**, *418*, 164.
- [31] D. Neagu, G. Tsekouras, D. N. Miller, H. Menard, J. T. Irvine, *Nat. Chem.* **2013**, *5*, 916.
- [32] D. Neagu, T. S. Oh, D. N. Miller, H. Menard, S. M. Bukhari, S. R. Gamble, R. J. Gorte, J. M. Vohs, J. T. Irvine, *Nat. Commun.* **2015**, *6*, 8120.
- [33] R. Shiozaki, A. G. Andersen, T. Hayakawa, S. Hamakawa, K. Suzuki, M. Shimizu, K. Takehira, *J. Chem. Soc.* **1997**, *93*, 3235.
- [34] W. Kobsiriphat, B. Madsen, Y. Wang, M. Shah, L. Marks, S. Barnett, *J. Electrochem. Soc.* **2009**, *157*, B279.
- [35] L. Ye, M. Zhang, P. Huang, G. Guo, M. Hong, C. Li, J. T. Irvine, K. Xie, *Nat. Commun.* **2017**, *8*, 14785.
- [36] K. Kousi, D. Neagu, L. Bekris, E. I. Papaioannou, I. S. Metcalfe, *Angew. Chem.* **2020**, *132*, 2531.
- [37] O. Kwon, S. Sengodan, K. Kim, G. Kim, H. Y. Jeong, J. Shin, Y. W. Ju, J. W. Han, G. Kim, *Nat. Commun.* **2017**, *8*, 15967.
- [38] H. Arandiyani, Y. Wang, J. Scott, S. Mesgari, H. Dai, R. Amal, *ACS Appl. Mater. Interfaces* **2018**, *10*, 16352.
- [39] C. Arrivé, T. Delahaye, O. Joubert, G. Gauthier, *J. Power Sources* **2013**, *223*, 341.
- [40] Z. Du, H. Zhao, S. Yi, Q. Xia, Y. Gong, Y. Zhang, X. Cheng, Y. Li, L. Gu, K. Swierczek, *ACS Nano* **2016**, *10*, 8660.
- [41] W. Qi, C. Ruan, G. Wu, Y. Zhang, Y. Wang, K. Xie, Y. Wu, *Int. J. Hydrogen Energy* **2014**, *39*, 5485.
- [42] Y. Zhu, W. Zhou, R. Ran, Y. Chen, Z. Shao, M. Liu, *Nano Lett.* **2016**, *16*, 512.
- [43] H. Tanaka, M. Uenishi, M. Taniguchi, I. Tan, K. Narita, M. Kimura, K. Kaneko, Y. Nishihata, *Catal. Today* **2006**, *117*, 321.
- [44] C. Duan, R. J. Kee, H. Zhu, C. Karakaya, Y. Chen, S. Ricote, A. Jarry, E. J. Crumlin, D. Hook, R. Braun, N. P. Sullivan, R. O'Hayre, *Nature* **2018**, *557*, 217.
- [45] M. T. Caldes, K. V. Kravchik, M. Benamira, N. Besnard, V. Gunes, O. Bohnke, O. Joubert, *Chem. Mater.* **2012**, *24*, 4641.
- [46] D. Han, S. Uemura, C. Hiraiwa, M. Majima, T. Uda, *ChemSusChem* **2018**, *11*, 4102.
- [47] J. Y. Park, Y. Zhang, M. Grass, T. Zhang, G. A. Somorjai, *Nano Lett.* **2008**, *8*, 673.
- [48] J. T. S. Irvine, D. Neagu, M. C. Verbraken, C. Chatzichristodoulou, C. Graves, M. B. Mogensen, *Nat. Energy* **2016**, *1*, 15014.
- [49] E. Gorbova, V. Maragou, D. Medvedev, A. Demin, P. Tsiakaras, *J. Power Sources* **2008**, *181*, 292.
- [50] S. M. Choi, J.-H. Lee, H. I. Ji, K. J. Yoon, J.-W. Son, B.-K. Kim, H. J. Je, H.-W. Lee, J.-H. Lee, *J. Solid State Electrochem.* **2013**, *17*, 2833.
- [51] K.-Y. Park, Y. Seo, K. B. Kim, S.-J. Song, B. Park, J.-Y. Park, *J. Alloys Compd.* **2015**, *639*, 435.
- [52] P. Babilo, S. M. Haile, *J. Am. Ceram. Soc.* **2005**, *88*, 2362.
- [53] O. Kosasang, R. Jareun, S. Phongsathit, S. Mach-mumas, *J. Aust. Ceram. Soc.* **2020**, *56*, 441.
- [54] D. Neagu, V. Kyriakou, I.-L. Roiban, M. Aouine, C. Tang, A. Caravaca, K. Kousi, I. Schreur-Piet, I. S. Metcalfe, P. Vernoux, *ACS Nano* **2019**, *13*, 12996.
- [55] R. Thalinger, M. Gocyla, M. Heggen, B. Klötzer, S. Penner, *J. Phys. Chem. C* **2015**, *119*, 22050.
- [56] L. A. Klinkova, V. I. Nikolaichik, N. V. Barkovskii, K. V. Van, V. K. Fedotov, *Russ. J. Inorg. Chem.* **2011**, *56*, 513.
- [57] G. Voronin, S. Degterov, *J. Solid State Chem.* **1994**, *110*, 50.
- [58] E. Zimmermann, K. Hack, A. Mohammad, A. Boudéne, D. Neuschütz, *Calphad* **1995**, *19*, 179.
- [59] W. Zhang, K. Osamura, S. Ochiai, *J. Am. Ceram. Soc.* **1990**, *73*, 1958.
- [60] T. Lindemer, E. Specht, *Phys. C* **1995**, *255*, 81.
- [61] Y. Song, W. Wang, L. Ge, X. Xu, Z. Zhang, P. S. B. Juliao, W. Zhou, Z. Shao, *Adv. Sci.* **2017**, *4*, 1700337.
- [62] J. B. Heywood, *Prog. Energy Combust. Sci.* **1976**, *1*, 135.
- [63] R. J. Gorte, J. M. Vohs, *Curr. Opin. Colloid Interface Sci.* **2009**, *14*, 236.
- [64] E. I. Papaioannou, D. Neagu, W. K. Ramli, J. T. Irvine, I. S. Metcalfe, *Top. Catal.* **2019**, *62*, 1149.
- [65] T. S. Oh, E. K. Rahani, D. Neagu, J. T. Irvine, V. B. Shenoy, R. J. Gorte, J. M. Vohs, *J. Phys. Chem. Lett.* **2015**, *6*, 5106.
- [66] S. Royer, D. Duprez, *ChemCatChem* **2011**, *3*, 24.